

Discrete transforms of quantized persistence diagrams

Michael E. Van Huffel* Olympio Hacquard† Vadim Lebovici‡ Matteo Palo§

Abstract

Topological data analysis leverages topological features to analyze datasets, with applications in diverse fields like medical sciences and biology. A key tool of this theory is the persistence diagram, which encodes topological information but poses challenges for integration into standard machine learning pipelines. We introduce QUPID (QUantized Persistence and Integral transforms of Diagrams), a novel and simple method for vectorizing persistence diagrams. First, QUPID uses a binning procedure to turn persistence diagrams into finite measures on a grid and then applies discrete transforms to these measures. Key features are the choice of log-scaled grids that emphasize information contained near the diagonal in persistence diagrams, combined with the use of discrete transforms to enhance and efficiently encode the obtained topological information. We conduct an in-depth experimental analysis of QUPID, showing that the simplicity of our method results in very low computational costs while preserving highly competitive performances compared to state-of-the-art methods across numerous classification tasks on both synthetic and real-world datasets. Finally, we provide experimental evidence that our method is robust to a decrease in the grid resolution used.

The code used to reproduce all the experiments is available at <https://github.com/majkevh/qupid>.

1 Introduction

Topological data analysis is a branch of machine learning that consists of extracting topological and geometric information to help analyze datasets. This information can be easily included in a workflow to perform various learning tasks on the data. As a result, these techniques have found applications in fields as diverse as medical sciences [1, 2, 3], biology, [4, 5], material sciences, [6, 7], cosmology [8], music theory [9, 10] and many more. A

central topological descriptor of this theory is the persistence diagram. Mathematically, a persistence diagram is a point cloud—that is, a finite subset—of \mathbb{R}^2 , where each point relates to and gives quantitative information on a topological feature of the data. Persistence diagrams can be computed from a wide spectrum of input data, including point clouds, graphs, images or time series. One natural approach is to replace raw input data with their persistence diagrams in classical machine learning analyses—such as regression or classification tasks—to focus on the topological and geometric information contained in data.

Due to their point cloud nature, persistence diagrams cannot be straightforwardly embedded in most standard machine learning algorithms. Several methods have been proposed to overcome this difficulty, such as neural network architectures pioneered in [11], or works based on optimal transport as in [12, 13].

Due to the topological information they carry, there has been a growing interest in proposing point cloud learning methods specifically tailored to persistence diagrams. Apart from some methods that perform learning directly at the point cloud level such as [14], most aim at mapping persistence diagrams into a vector space. Following this vectorization step, any off-the-shelf machine learning algorithm suited to the task to perform (e.g., classification, regression, or clustering) can be used. In [15] for instance, persistence diagrams are turned into so-called *persistence images*, which consist of the pixelization of a convolution of the point cloud with a Gaussian kernel. Some methods such as [16] and [17] have used kernel-based algorithms. More recently, neural network-based vectorizations have been proposed, such as [18] and [19]. Finally, let us mention ATOL [20], which uses a clustering algorithm on persistence diagrams to find points of interest and takes the mass around each cluster centre as coordinates for the vectorization.

Contributions. We introduce a new vectorization methodology for persistence diagrams called QUPID (QUantized Persistence and Integral transforms of Diagrams). First, we turn persistence diagrams into finite measures on a user-chosen grid via a binning procedure. Second, we apply a discrete integral transform (e.g. Fourier, wavelet) to these measures to extract and

*Department of Mathematics, ETH Zurich, Switzerland, michavan@student.ethz.ch

†KUIAS, Kyoto University, Japan, hacquard.olympio.47i@st.kyoto-u.ac.jp

‡Mathematical Institute, University of Oxford, United Kingdom, vadim.lebovici@maths.ox.ac.uk

§Department of Mathematics, ETH Zurich, Switzerland, mapalo@student.ethz.ch

enhance valuable structure patterns in persistence diagrams.

We claim that the strength of our method lies in its great simplicity. We show that this simplicity translates into reduced computational time. We obtain very competitive accuracy results in supervised classification tasks while being several times faster than persistence images and kernel methods; and being dramatically faster than neural networks. In particular, we validated our model on a real-world dataset of tumour immune cell type classification. Finally, combining the classical knowledge of discrete transforms and the structure of persistence diagrams, the simplicity of our method allows for straightforward interpretations of the output vector representation.

We interpret the promising results of QUPID as due to three key features. First, our binning procedure greatly emphasises regions of persistence diagrams with a high density of points, which typically correspond to regions where fine geometric information on data is experimentally proven to be contained; see Section 3.1 for more details. Second, we leverage the flexibility of our method in the possibility of choosing log-scaled grids that further emphasise the high-density regions in persistence diagrams. Doing so, QUPID becomes a vectorization of point clouds specifically adapted, but not restricted to, persistence diagrams. Third, in comparison with the quite similar ATOL algorithm, the possibility to choose any discrete transform allows for additional flexibility and a clear improvement in feature extraction from persistence diagrams.

Outline. Section 2 introduces basic notions of topological data analysis and persistence diagrams, emphasizing why they are relevant data descriptors. Section 3 describes the algorithm QUPID to turn persistence diagrams into vectors. Finally, Section 4 presents numerous experiments on synthetic and real-world datasets, showing that QUPID reaches a very competitive accuracy when benchmarked against state-of-the-art methods. In addition, this section provides a thorough analysis of our method, its computational efficiency, and the influence of the resolution of the grid used in the quantization.

2 Background on topological data analysis

Throughout this paper, we develop an algorithm for fast learning on point cloud data. The main emphasis will be the classification of topological descriptors called persistence diagrams. In this section, we describe their construction and build intuition on the type of information they capture.

Starting from diverse input data (graphs, images, point clouds, time series...), topological data analysis

aims at extracting topological information, that is, the homotopy type of some underlying geometric object the data is assumed to lie on. The main tool to do so is *homology* from algebraic topology. Doing so with a multi-scale approach is the purpose of *persistent homology*, as introduced in the reference textbooks [21, 22].

Intuitively, given a topological space X , the k -th homology of X is a vector space whose dimension is equal to the number of independent k -dimensional holes of X for $k \geq 1$ (loops for $k = 1$, voids for $k = 2$ and so on) and to the number of connected components for $k = 0$. Given a nested family of topological spaces $\mathcal{X} = (X_t)_{t \in \mathbb{R}}$ called a *filtration* (i.e., such that $X_{t_1} \subset X_{t_2}$ whenever $t_1 < t_2$), the degree- k persistent homology tracks the evolution of the degree- k homological features—i.e., the generators of the k -th homology of X_t as the parameter t increases.

We denote by \mathcal{D} the set of finite multi-sets of points $(a, b) \in \mathbb{R}^2$ such that $a \leq b$, called *persistence diagrams*. To a filtration \mathcal{X} and an integer $k \geq 0$ one can associate a persistence diagram $D \in \mathcal{D}$ composed of the collection of all couples (a, b) such that a given degree- k homological feature is born at parameter $t = a$ and dies at parameter $t = b$ in the filtration \mathcal{X} .

Given raw input data, the choice of filtration is central and will determine the aspect of the persistence diagram. If the input data is a point cloud $\mathbf{X} = (x_i)_{i=1}^n$ in \mathbb{R}^d , a widespread choice of filtration is given by the union of balls centred around each data point for increasing radius $t \in \mathbb{R}_{\geq 0}$, called the *Čech filtration* and denoted by $\check{C}(\mathbf{X}, t) = \cup_{i=1}^n B(x_i, t)$ for each $t \in \mathbb{R}_{\geq 0}$. We therefore have d persistence diagrams corresponding to topological features of dimensions $0, 1, \dots, d-1$. Unless specified otherwise, this is the filtration we will use when processing point cloud data in Section 4.

We show an example of the construction of a persistence diagram for the Čech filtration of a point cloud of \mathbb{R}^2 in Figure 1. In this example, the points are sampled on two circles of different radius. Once the radius in the Čech filtration is large enough, two cycles appear successively. These topological features exist until the radius parameter becomes large enough and the union of balls fills each circle. Hence, we observe two points significantly away from the diagonal in the degree-1 persistence diagram, corresponding to the two circles in the original data, as well as numerous points lying close to the diagonal. We remark that the 0-persistence diagram is a one-dimensional object. Indeed, there are as many connected components as points in the initial data. They are all born at time 0 and die successively by merging with neighbouring points, such that they can be encoded using only their

death time.

We define the *persistence* of a feature (b, d) in the diagram as the real number $d - b$, corresponding to its lifetime. The situation from Figure 1 is typical. Indeed, it is now well-understood that the persistence diagram of a Čech filtration is composed of a few points of high persistence on the one hand, corresponding to global homological features of the input point cloud, and a large clump of points of low persistence on the other hand, corresponding to local and sampling effects. We refer to [14] for a more detailed overview.

Finally, note that as observed in [23], a persistence diagram $D \in \mathcal{D}$ can be equivalently expressed as a discrete measure μ_D over \mathbb{R}^2 , called *persistence measure* of D , defined as the sum of Dirac masses centred on each point of the diagram $\mu_D = \sum_{(b,d) \in D} \delta_{(b,d)}$. This measure-theoretic approach has led to many developments in the structure of the space of persistence diagrams, see [24].

3 Methodology

An objective of topological data analysis is to extract predictions from the persistence diagrams. Unfortunately, given their mathematical nature as a multi-set of points (or a discrete measure), they cannot directly replace the raw data as input of standard machine learning algorithms. Indeed, they almost always require the data to be elements of a vector space. A common strategy is therefore to map the persistence diagrams in \mathbb{R}^n where the dimension n is typically chosen by the user. This initial data-transformation step is commonly referred to as the *vectorization step*. We refer to [25] for a survey of different vectorization methods in topological machine learning.

In this section, we introduce the QUPID vectorization algorithm. It proceeds in two steps:

$$\text{QUPID: } \mathcal{D} \xrightarrow{\mathfrak{q}} \mathcal{M}_G \xrightarrow{\Psi} \mathbb{C}^n,$$

where the first step $\mathfrak{q}: \mathcal{D} \rightarrow \mathcal{M}_G$ is a quantization step sending a persistence diagram to a finite measure supported on a fixed grid G (Section 3.1), and the second step $\Psi: \mathcal{M}_G \rightarrow \mathbb{C}^n$ is a discrete transform (Section 3.2) that outputs a vector in a Euclidean space of dimension n . See Figure 2 for an illustration.

3.1 Quantized persistence diagrams Let $D \in \mathcal{D}$ be a persistence diagram. The *persistence diagram in birth-persistence coordinates* associated to D is the image D^\perp of D by the map $(b, d) \mapsto (b, d - b)$. The grid used for quantized persistence diagrams will be associated with two finite sets of non-negative real numbers $\mathcal{B} = \{b_1 < \dots < b_r\}$ and $\mathcal{P} = \{p_1 < \dots < p_s\}$. Denote $G = \{1, \dots, r\} \times \{1, \dots, s\}$ and by \mathcal{M}_G the space

of finite measures supported on G . The quantization of persistence diagrams is a simple binning process:

DEFINITION 3.1. *The quantization of D with respect to $(\mathcal{B}, \mathcal{P})$ is the finite measure $\mathfrak{q}\mu_D \in \mathcal{M}_G$ defined by:*

$$\mathfrak{q}\mu_D = \sum_{(i,j) \in G} m_{i,j} \delta_{(i,j)},$$

where, setting $b_{r+1} = p_{s+1} = +\infty$ and denoting by $\mathbf{1}_Z: \mathbb{R}^2 \rightarrow \{0, 1\}$ the indicating function of $Z \subset \mathbb{R}^2$,

$$\begin{aligned} m_{i,j} &= \langle \mu_D, \mathbf{1}_{[b_i, b_{i+1}) \times [p_j, p_{j+1})} \rangle \\ &= \#\{(b, p) \in D^\perp : b_i \leq b < b_{i+1} \\ &\quad \text{and } p_j \leq p < p_{j+1}\}. \end{aligned}$$

In our experiments, we will exploit the flexibility of our methodology concerning the choice of finite sets $\mathcal{B} = \{b_1 < \dots < b_r\}$ and $\mathcal{P} = \{p_1 < \dots < p_s\}$. The first obvious choice is to uniformly sample values between the extremal values attained by the persistence diagrams in birth-persistence coordinates computed from data. We refer to this choice as a *uniform grid*. The second one, called *log-scaled grid*, is to apply a scaling function to the birth-persistence space before the quantization step, namely the function $(b, p) \mapsto \log(1 + b\alpha_1 + p\alpha_2)$ for some $\alpha = (\alpha_1, \alpha_2)$ with $\alpha_1, \alpha_2 > 0$. See Figures 2a to 2c for an illustration.

Our methodology is designed to emphasize low persistence points. First, as explained in Section 2, persistence diagrams typically contain few high-persistence points and numerous low-persistence points. Thus, as illustrated in Figure 2, the few high persistence points in the persistence diagrams will be significantly shaded in the binning process by the high multiplicities of low persistence regions. Moreover, the ability to choose an appropriate rescaling parameter α in log-scaled grids provides quantized persistence diagrams with finer resolution in low persistence regions.

This emphasis on low-persistence points will be key to our experimental results in Section 4. Indeed, if historically considered noise as in [15], low persistence points are now considered as containing crucial information on data, see [26] and [14]. In point cloud analysis, for instance, low persistence points are tightly connected to pairwise distances between points of the point cloud, retaining a lot of geometric and sampling-related information. These considerations have been used in curvature regression tasks [26, 19, 27] or in the unsupervised classification of geometric patterns in background noise [27]. The experiments in Section 4 aim to provide new evidence in this direction.

Remark that our method is quite similar to the ATOL method from [20]. One of the main differences

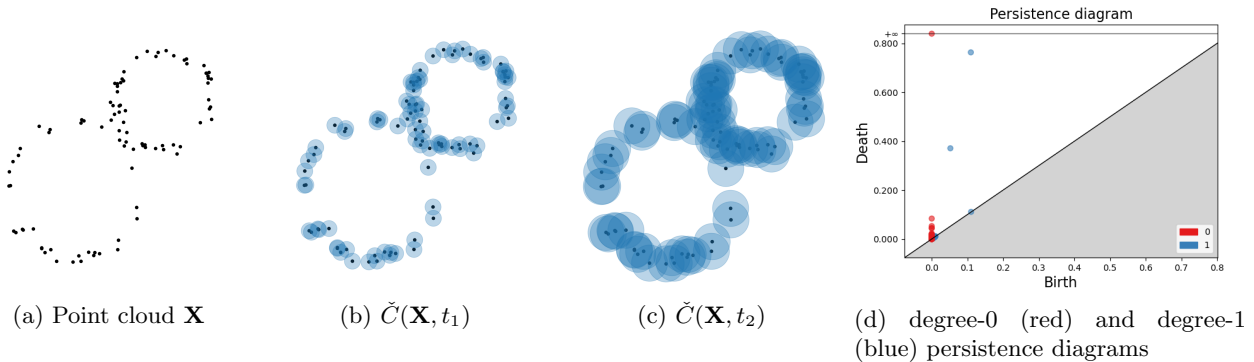


Figure 1: Union of balls at radii t_1 (b) and t_2 (c) with $t_1 < t_2$ centred on a point cloud sampled around two circles (a). Taking every radius t defines the Čech filtration and the corresponding persistence diagrams (d).

lies in the way low-persistence features are emphasized: we chose an adaptive-grid approach where the scaling parameter is optimized during the learning process. On the contrary, ATOL runs a clustering algorithm on the data such that their binning process is fully independent of the data's labels. In addition, taking a large class of integral transforms allows us for a more diverse data exploration, that can result in a quite strong accuracy gain in some tasks. We refer in particular to Section 4.3.

3.2 Discrete transforms In this section, we briefly recall some classical notions from the theory of discrete transforms and refer to [28] for further details. Consider a finite grid $G = \{1, \dots, r\} \times \{1, \dots, s\} \subset \mathbb{R}^2$ as in Section 3.1. We denote by $n = r \times s$ the resolution of the grid. The grid is chosen by the user and its resolution n has a central importance as it acts as a trade-off between the computational efficiency and numerical accuracy of the method. We let $\{\psi_l\}_{1 \leq l \leq n}$ be a family of square-integrable complex-valued functions on \mathbb{R}^2 .

DEFINITION 3.2. *The discrete transform associated to $\{\psi_l\}$ of the finite measure $\nu \in \mathcal{M}_G$ is the complex vector $\Psi(\nu) \in \mathbb{C}^n$ with coordinates:*

$$\Psi(\nu)_l = \langle \nu, \psi_l \rangle.$$

We consider three types of discrete transforms $\Psi: \mathcal{M}_G \rightarrow \mathbb{C}^n$.

Identity. The identity transform $\text{Id}: \mathcal{M}_G \rightarrow \mathbb{R}^n$ is associated to the family $\{\psi_{i,j}\} = \{\mathbf{1}_{[b_i, b_{i+1}) \times [p_j, p_{j+1})}\}$ induced by the finite sets \mathcal{B} and \mathcal{P} . In that case, denoting the finite measure $\nu = \sum_{(i,j) \in G} m_{i,j} \delta_{(i,j)}$ for real numbers $m_{i,j}$, we have $\Psi(\nu)_{i,j} = \langle \nu, \psi_{i,j} \rangle = m_{i,j}$. Therefore, as its name suggests, the identity transform $\Psi(\nu)$ is just another way of storing the

finite measure ν . We denote it by QUPID-id in our experiments.

Fourier. The *discrete Fourier transform* $\mathcal{F}: \mathcal{M}_G \rightarrow \mathbb{C}^n$ is associated to the family $\{\psi_{l_1, l_2}\}$ where $\psi_{l_1, l_2}(i, j) = \exp(-i2\pi(l_1 \frac{i}{r} + l_2 \frac{j}{s}))$; see [28, Sec. 3.4]. This transform is computed using the Fast Fourier Transform algorithm [29]. The magnitude and phase of the output are flattened and concatenated to form the vectorization we use in our experiments, denoted by QUPID-fft.

Wavelets. The last type of transforms used in this article are discrete wavelet transforms, namely, the Daubechies and Coiflet transform; see [28, Chap. 7] and [30]. The definition of wavelets on the two-dimensional plane is made precise in [28, Thm. 7.25]. The *Daubechies* and *Coiflet wavelet transforms of order p* are associated to families of wavelets satisfying specific theoretical properties. Namely, the Daubechies wavelets of order p have p vanishing moments [28, (7.69)] and have minimal support with this property [28, Thm. 7.7]. The Coiflet wavelets of order p have minimal support with p vanishing moments and such that their so-called *scaling function* [28, Sec. 7.1.2] are normalized and have $p - 1$ vanishing moments.

The choice of the order p yields different wavelets, hence allowing for further flexibility in our framework. When $p = 1$, the Daubechies wavelet transform coincides with the simpler *Haar wavelet transform*; see [28, Sec. 7.2.2]. We provide the explicit definition of the Haar transform below. Defining the following two functions $\psi = \mathbf{1}_{[0,1/2)} - \mathbf{1}_{[1/2,1)}$ and $\phi = \mathbf{1}_{[0,1)}$, the Haar wavelet transform is associated to the family of wavelets

$\{\psi_{k,l_1,l_2}^V, \psi_{k,l_1,l_2}^H, \psi_{k,l_1,l_2}^D\}_{(k,l_1,l_2) \in \mathbb{Z}^3}$ where:

$$\begin{aligned}\psi_{k,l_1,l_2}^V(x_1, x_2) &= \frac{1}{2^k} \phi\left(\frac{x_1 - 2^k l_1}{2^k}\right) \psi\left(\frac{x_2 - 2^k l_2}{2^k}\right), \\ \psi_{k,l_1,l_2}^H(x_1, x_2) &= \frac{1}{2^k} \psi\left(\frac{x_1 - 2^k l_1}{2^k}\right) \phi\left(\frac{x_2 - 2^k l_2}{2^k}\right), \\ \psi_{k,l_1,l_2}^D(x_1, x_2) &= \frac{1}{2^k} \psi\left(\frac{x_1 - 2^k l_1}{2^k}\right) \psi\left(\frac{x_2 - 2^k l_2}{2^k}\right).\end{aligned}$$

In our experiments, we use the `Python` library `PyWavelets` to compute discrete transforms. For the Haar wavelets, taking as input a finite measure $\nu \in \mathcal{M}_G$ (such as quantized persistence diagram) seen as a two-dimensional array, this library outputs the vector $\Psi(\nu)$ of Definition 3.2 associated to the family

$$(3.1) \quad \{\psi_{1,l_1,l_2}^V, \psi_{1,l_1,l_2}^H, \psi_{1,l_1,l_2}^D\}_{(l_1,l_2) \in \mathbb{Z}^2}$$

obtained for $k = 1$, called respectively *vertical*, *horizontal* and *diagonal details*. In addition, it outputs the vector of *approximation coefficients* obtained for the family:

$$\psi_{1,l_1,l_2}^A(x_1, x_2) = \frac{1}{2} \phi\left(\frac{x_1 - 2l_1}{2}\right) \phi\left(\frac{x_2 - 2l_2}{2}\right).$$

In practice, we concatenate horizontal, vertical, and diagonal details and approximation coefficients into a vectorization of the input measure ν . We proceed similarly for the other Daubechies and Coiflet wavelets of order p , respectively denoted by `QUPID-dbp` and `QUPID-coifp` in our experiments. Of course, one could get finer vectorizations by considering larger subfamilies than the one from (3.1), including other values of $k \in \mathbb{Z}$.

3.3 Algorithmic complexity One of the main strengths of QUPID is its computational simplicity. Given a persistence diagram with l points, the quantization step consists solely of a binning process, hence will run in $\mathcal{O}(l)$ operations independently of the size $n = r \times s$ of the grid used for the quantization. The total time complexity of QUPID will therefore be of $\mathcal{O}(l + n \log(n))$ for the Fast Fourier Transform [29] and of $\mathcal{O}(l + n)$ for a Fast Wavelet Transform [31]. It is to be noted that according to [32], in some random settings, the number of points l in the persistence diagram of a Čech filtration of a randomly sampled point cloud in the Euclidean space will asymptotically be of the same order as the number of points in the initial point cloud.

This is to be paralleled by the computational complexity of computing persistence diagrams. For computational reasons, we do not use the Čech filtration in our experiments on point clouds but rather a homotopy equivalent one called the *alpha filtration*; see [33]. Doing so, computing any degree persistence diagram from

a point cloud with N points in \mathbb{R}^d has a time complexity of $\mathcal{O}(N^{d\omega/2})$ in the worst case, where $2 \leq \omega \leq 2.373$ is the matrix multiplication time; see [34, 35].

Taken together, this assesses that the computational cost of our vectorization is expected to be much smaller than the computation of persistence diagrams themselves. We will back up these theoretical claims by timing experiments in Section 4.1 by comparing our method with standard persistence diagrams vectorizations and showing that QUPID benefits from a reduced computational cost in practice.

4 Experiments

In this section, we evaluate the vectorization procedure of QUPID by performing a classification task on some synthetic and real-world datasets. The typical workflow is the following: starting from a raw data input, we compute persistence diagrams using the `gudhi` library [36]. We then apply QUPID for all possible transforms and a user-given grid resolution. Unless explicitly mentioned otherwise, the classification task itself is performed with a random forest classifier [37] using the implementation from the `scikit-learn` library [38]. The code to reproduce the experiments is available at <https://github.com/majkevh/qupid>.

In what follows, we specify the transform used in every accuracy table or write QUPID* for the accuracy corresponding to the transform reaching maximum accuracy among all the ones tried.

4.1 Dynamical system (ORBIT5K dataset) The ORBIT5K dataset is a commonly used benchmark for supervised classification tasks in topological data analysis [15, 17, 16, 14, 18, 20, 27]. It is a synthetic dataset consisting of point clouds of a thousand points in the unit square $[0, 1]^2$, generated by a dynamical system depending on a real parameter $\rho > 0$. For each point cloud, the first point (x_0, y_0) is drawn uniformly at random in the unit square, and the remaining points (x_n, y_n) for $n = 1, \dots, 999$ are generated recursively by the formula:

$$\begin{aligned}x_n &= x_{n-1} + \rho y_{n-1}(1 - y_{n-1}) && \text{mod } 1, \\ y_n &= y_{n-1} + \rho x_n(1 - x_n) && \text{mod } 1.\end{aligned}$$

The whole dataset consists of five classes, each of a thousand point clouds, for five values of the parameter $\rho \in \{2.5, 3.5, 4.0, 4.1, 4.3\}$. See Figure 3 for an illustration.

Supervised classification. The dataset is divided by a 70/30 randomized train/test split for each class. Changing the parameter ρ changes the underlying topology and sampling distribution of the generated orbits. We try to predict the value of ρ given the point cloud as data. We compare two vectorizations based on

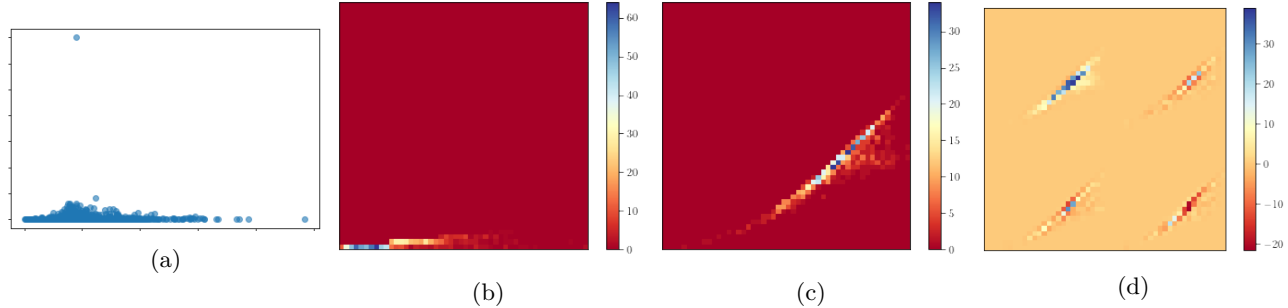


Figure 2: An example of degree-1 persistence diagram in birth-persistence coordinates obtained from the Čech filtration of a point cloud (a), its associated quantized persistence diagram with regular grid of size 50×50 (b), its associated quantized diagram with log-scaled grid of size 50×50 and parameter $\alpha = (500, 500)$ (c), and the discrete Daubechies transform of order 2 (with approximation coefficients, vertical, horizontal, diagonal details from top left to bottom right) of this quantized diagram (d).

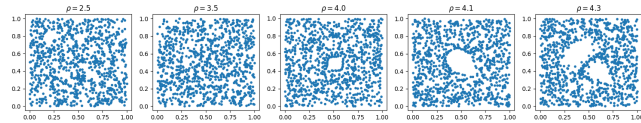


Figure 3: Examples of point clouds from the ORBIT5K dataset.

our methodology described in Section 3. We begin by computing degree-0 and degree-1 persistence diagrams of the Čech filtration computed on the point clouds as described in Section 2. As mentioned in Section 3.3, we use alpha-filtrations instead of Čech filtrations for computational reasons; see [33]. We consider an adaptive log-scaled grid with a parameter α chosen by grid search cross-validation, coupled with the Fourier transform and the Daubechies and Coiflet wavelet transforms of orders 1, 2 and 3. We also considered the identity transform over a uniform grid, noticing that the choice of an adaptive grid gave highly sub-optimal results. Our accuracies are averaged over ten runs and reported for the transform reaching higher accuracy (Coiflet of order 2 in this case) in Table 1. Additional results for other discrete transforms are available in the appendix (Table 6).

In Table 1, we also compare our method with three state-of-the-art vectorizations of persistence diagrams. Namely, Persistence Images (PI) [15], Persistence Fisher Kernels (PF-K) [17] and Persformer [19].

On this classification task, taking wavelet transforms induces a significant gain in accuracy allowing QUPID to reach a state-of-the-art accuracy. It is only outperformed by the Persformer method which relies on the costly training of a neural network with transformer architecture. In comparison, our method is faster to

PI*	PF-K [†]	Persformer*	QUPID [★] *	QUPID-id*
82.5	85.9 ± .8	91.2 ± .8	88.3 ± .4	82.0 ± .6

Table 1: Classification scores for the ORBIT5K dataset. Notes: [†] denotes methods with accuracy averaged over 100 runs; * indicates averaging over 10 runs; * signifies an average over 5 runs. No standard deviation is reported in [15] for persistence images.

compute than all other methods, as shown in the following paragraph.

Finally, let us also point out that applying QUPID-id directly on the point cloud without any homology computation yields an accuracy of around 99%, similar to what was observed in [20, 19]. Therefore, this experiment should be considered only as a proof-of-concept to benchmark our method against other vectorizations of persistence diagrams.

Timing. All computations were conducted on a single laptop, an Apple M3 Pro equipped with an 11-core CPU and no GPU. The main strength of our method lies in its simplicity, which translates into a very meagre computational cost while still keeping a competitive accuracy. This is shown in Table 2 where we report the time to vectorize the ORBIT5K dataset for all methods cited in Table 1. We use a resolution of 32×32 for persistence images (PI) and QUPID with log-scaled grids, and the PF-K vectorization is timed with default parameters. Computational times for Persformer are not provided in [19] and training this Transformer architecture on our CPU was impossible in a reasonable time. Still, the authors of the paper have shared with us in a private communication that the training process takes in the order of hours on GPUs, which we report in the table.

Vectorization	Time
QUPID-id	15 s
QUPID-fft	17 s
QUPID-db2	15 s
QUPID-coif2	16 s
PF-K	69 s
PI	74 s
Persformer	~ hours

Table 2: Time to vectorize the ORBIT5K dataset.

First, note that considering discrete Fourier or wavelet transforms has a negligible cost compared to the quantization process itself. Overall, the results of Tables 1 and 2 show the excellent accuracy-complexity trade-off of QUPID. On the one hand, our method allows for an increase of almost 3% in accuracy with a computational time divided by more than 4 for PI and PF-K. On the other hand, our method takes only a dozen of seconds on a CPU against hours for Persformer on a GPU at the cost of only 3% in accuracy.

4.2 Graph classification All the previous examples dealt with point clouds as input data. Topological data analysis can take a much larger class of input data, such as graphs. In this section, we consider a supervised graph classification problem. To compute the persistence diagrams of a graph, we need to introduce a topological filtration. A common choice initiated in [18] is to introduce the heat kernel signature of a graph:

DEFINITION 4.1. *For a graph $\mathcal{G} = (V, E)$, the Heat Kernel Signature (HKS) function with diffusion parameter $t > 0$ is defined for each vertex $v \in V$ as*

$$\text{HKS}_t(v) = \sum_{k=1}^{|V|} \exp(-t\lambda_k) \psi_k(v)^2,$$

where λ_k is the k -th eigenvalue of the normalized graph Laplacian, and ψ_k is the corresponding eigenfunction.

The heat kernel signature at a vertex v can be interpreted as the remaining heat at v starting from a unit heat distribution on v after a time t has elapsed; see [39]. The HKS carries a lot of local and global structural information on the graph, related to its connectivity and topology. The HKS defines a function on the set of vertices that can be simply extended to the set of edges. If $e = (x, y)$ is an edge between vertices x and y , we set $\text{HKS}_t(e) = \max(\text{HKS}_t(x), \text{HKS}_t(y))$. For a given parameter t , considering the graphs given by the sublevel sets or superlevel sets of the HKS gives us a topological filtration.

We adopt the same methodology as in [18] and [20], where taking the degree-0 and degree-1 persistence diagrams both for the sublevel sets and superlevel sets of the HKS provides us with a family of four persistence diagrams per graph called *extended persistence*.

We benchmark our method with state-of-the-art graph classification algorithms on a few real-world datasets. The datasets include the social graphs IMDB-B, IMDB-M, COLLAB, REDDIT-5K and REDDIT-12K, as well as graphs coming from chemoinformatics and bioinformatics, namely COX2, DHFR, MUTAG and PROTEINS.

We adopt the methodology from [20] for generating extended persistence diagrams, using two specific HKS diffusion times ($t_1 = 0.1$ and $t_2 = 10$), focusing solely on the topological structure without considering additional graph attributes. Therefore, we end up with eight persistence diagrams and concatenate all corresponding vectorizations obtained from QUPID. For the evaluation, we used three distinct regular grid sizes 20×20 , 32×32 , and 50×50 across all our proposed transforms except for the COLLAB and REDDITs datasets where we used only 10×10 and 20×20 . Regarding the wavelet transforms, we experimented with six different wavelet types, namely Daubechies and Coiflet of orders 1, 2 and 3. The highest accuracy achieved over these transforms (QUPID \star) is presented in Table 3. Detailed accuracy for each transform across the different grids and standard deviations can be found in the appendix (Table 5). Performance is assessed through 10-fold evaluations on each dataset, reporting both average and best 10-fold results.

In Table 3, we also compare ourselves with state-of-the-art graph classification methods. In the first three columns, we compare with methods using neural networks or kernel methods. Namely, a scale-variant topological method (SV from [40]), a graph kernel method based on random walks (RetGK from [41]), a graph embedding method using spectral distances (FGSD from [42]), a Capsule Graph Neural Network (GCNN from [43]), and a Graph Isomorphism Network (GIN from [44]). In the three following columns, we compare our results with Persistence Images from [15] and Persistence Landscapes from [45] coupled with an XGboost classifier. The maximum accuracy of these two methods is denoted in the ‘‘P’’ column. We also compare ourselves with Perslay [18] and ATOL [20].

These results show that despite its apparent simplicity, QUPID achieves decent performances in all classification tasks. We always outperform persistence images and landscapes (P) and are comparable with other TDA-based vectorizations of persistence diagrams across all datasets. Importantly, we show very competi-

Dataset	SV [†]	RetGK [*]	FGSD [†]	GCNN [†]	GIN [†]	P [†]	Perslay [*]	ATOL [*]	QUPID [*]	
									Mean [*]	Max [†]
MUTAG	88.3	90.3	92.1	86.7	89.0	79.2	89.8	88.3	89.8	91.7
COX2	78.4	81.4	-	-	-	76.0	80.9	79.4	80.6	82.4
PROTEINS	72.6	75.8	73.4	76.3	75.8	65.4	74.8	71.4	72.8	73.6
DHFR	78.4	81.5	-	-	-	70.9	80.3	82.7	81.8	83.1
IMDB-B	72.9	71.9	73.6	73.1	74.3	54.0	71.2	74.8	68.2	69.3
IMDB-M	50.3	47.7	52.4	50.3	52.1	36.3	48.8	47.8	43.7	44.4
COLLAB	-	81.0	80.0	79.6	80.1	-	76.4	88.3	86.4	86.7
REDDIT-5K	-	56.1	47.8	52.9	57.0	-	55.6	67.1	66.1	66.6
REDDIT-12K	-	48.7	-	46.6	-	-	47.7	51.4	51.4	51.7

Table 3: Classification scores for graph datasets. Note: The symbol [†] indicates that the performance should be compared with the *max* metric, while the symbol ^{*} denotes that the comparison should be made with the *mean* metric.

tive performances on the COLLAB and REDDITs datasets, comparable to the ATOL algorithm, thus outperforming all other methods. This should be read in the light of the fact that, as explained in [20], those three datasets are considered the most difficult to classify due to their size in terms of number of data and number of edges and vertices.

4.3 Tumor immune cells We use our method to study a real-world dataset introduced in [46] which contains point clouds in \mathbb{R}^2 obtained from spatial locations of immune cells in tumours. The dataset contains three different types of immune cells, namely, $CD68^+$ (65 point clouds with average of 560 points, minimum of 88 and maximum of 1000), $FoxP3^+$ (74 point clouds with average of 211 points, minimum of 24 and maximum of 499) and $CD8^+$ (73 point clouds with average of 651 points, minimum of 194 and maximum of 1000). In [46], authors use the sophisticated machinery of *multiparameter persistent landscapes* to study this dataset for a multiparameter filtration, namely, position and local density of cells. Here, we study the same data using only one parameter, following our methodology introduced in Section 3, and used in Section 4.1. We compute degree-0 and degree-1 persistence diagrams associated with the Čech filtration (in fact, alpha filtration) and consider the QUPID vectorization.

Unsupervised setting. We start by considering the problem of unsupervisedly predicting the type of immune cell. We show in Figure 4 a t-SNE plot of QUPID using the Coiflet transform of order 2 on the degree-0 and degree-1 persistence diagrams. Our method satisfyingly separates the $FoxP3^+$ class from the two other classes suggesting that this class is easy to discriminate from the other two. This shows that QUPID already highlights discriminative information on

this dataset at the unsupervised level.

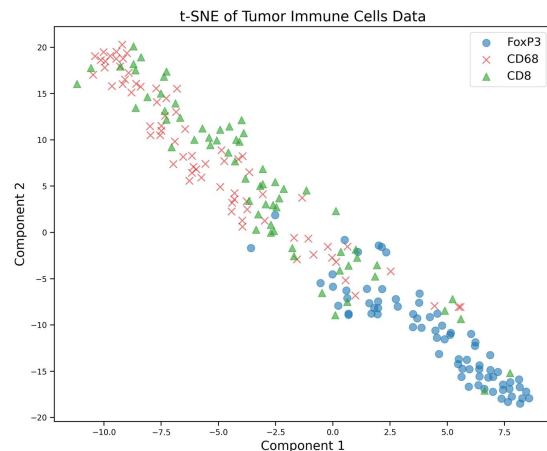


Figure 4: t-SNE plot of QUPID for the Coiflet transform of order 2 on the tumor immune cells dataset.

Supervised setting. We use our methodology in the supervised cell-type classification task and the three corresponding binary problems. We use the same setting as in Section 4.1 to vectorize persistence diagrams using QUPID, with adaptive log-scaled grids. We denote it by $QUPID_{PD}$. For each classification problem, we make a randomized 80/20 training/test split as in [46]. We report the results averaged over 20 runs in Table 4. Detailed accuracies for each transform across the different transforms can be found in the appendix (Table 7).

We also compare our vectorization of persistence diagrams with four other methods. First, we compare ourselves to scores reported in the original paper [46]

using multiparameter persistence landscapes (MPL), a topological descriptor using a two-parameter filtration. Second, we vectorize the raw point clouds using QUPID with a uniform grid of size 32×32 , comparing the same eight transforms: identity, Fourier, Daubechies ($p = 1, 2, 3$) and Coiflet ($p = 1, 2, 3$). We denote it by QUPID_{raw}. The last two methods consist in using ATOL [20] to vectorize the raw point clouds (ATOL_{raw}) or their persistence diagrams (ATOL_{PD}). We chose the ATOL budget-parameter giving the best accuracy. For every vectorization, we applied a random forest or an LDA classifier from the `scikit-learn` library and reported the best accuracy for each method in Table 4.

Task	MPL	ATOL _{PD}	ATOL _{raw}	QUPID _{PD} *	QUPID _{raw} *
CD68 vs CD8	65.3	61.1	51.4	79.0	65.0
CD68 vs FoxP3	86.3	90.7	87.7	98.2	89.2
CD8 vs FoxP3	74.7	85.9	85.7	96.3	87.7
All classes	66.2	67.3	58.5	79.4	67.9

Table 4: Comparative analysis of performance for immune cells classification task.

First, results of Table 4 demonstrate the advantage of considering persistence diagrams over raw point clouds, both for the QUPID and the ATOL vectorizations. This suggests that the topological and geometric information captured by persistence diagrams is relevant for this classification task.

Quantitatively, these results demonstrate the benefits of using the QUPID algorithm to vectorize persistence diagrams. Not only do we outperform ATOL vectorization of persistence diagrams in all tasks—and by more than 10% in all but one—, but we also outperform the multiparameter approach MPL by even larger amounts—22% in the case of CD8⁺ vs FoxP3⁺. We believe this is due to the ability of our method to focus on low-persistence points, allowing it to capture fine geometric information missed by other methods.

Timing. Finally, we report the computational times for all methods in this classification task. Computing multiparameter persistence landscapes on the entire dataset took approximately 3 hours, against a few seconds for QUPID and ATOL. Moreover, computing persistence diagrams is the most time-consuming task, with more than 1 second, against less than 0.5 seconds for the vectorization step.

Feature importance. To gain some interpretability, we compute the random forest’s feature importance of each coefficient of the vectorizations using `scikit-learn`. In Figure 5, we plot the feature importance heatmap of the QUPID-coif2 vectorization of persistence diagrams for the binary classification of CD68⁺ vs FoxP3⁺. We can see that both the degree-0 and degree-1 persistence diagrams are used in the classifica-

tion, but the former is only through its approximation coefficients and vertical detail. For degree-1 persistence, the approximation coefficients carry the most information, mainly through its early-birth features. The horizontal and vertical details also contain important information, extremely concentrated in a few coefficients. The possibility to make such an analysis is crucial in sensitive applications such as processing medical data, where we can directly relate the prediction to a few key-details in the wavelet analysis of topological descriptors.

4.4 Influence of the resolution parameter As demonstrated in the previous quantitative experiments, considering discrete transforms usually yields higher accuracy than using the identity transform in supervised tasks. To further stress this fact, we come back to the setting of Section 4.1 where we compare the accuracy of several transforms on a square grid of varying size; see Figure 6. A similar study has been conducted in [20, 27].

Naturally, increasing the resolution usually provides a higher accuracy. We notice that for this task, wavelet transforms offer better accuracy than the identity at every possible resolution and that the difference is even more striking at low resolutions. Indeed, benefiting from their signal-compression properties, wavelet transforms can offer a competitive accuracy using a very limited number of coefficients. This makes them a first-choice option when working under a limiting vectorization budget.

5 Conclusion and further work

This work falls within an old endeavour of mapping persistence diagrams into a vector space to use off-the-shelf statistical learning methods. We believe that the algorithm developed in this article allows us to take a step back from the existing literature and to realize that using a seemingly naive approach of binning the diagrams and using standard discrete transforms accounts for strong predictive power. More precisely, the take-home message of the QUPID algorithm is the following:

- We reach a very good accuracy in a wide variety of settings.
- The gap in accuracy with the most competitive methods is traded off by the extreme simplicity of the method and its reduced computational time.
- We successfully made use of log-scaled grids that focus on the low-persistence points, giving one more piece of evidence that the near-diagonal points carry a lot of discriminative information.
- In addition to improving the overall accuracy, using

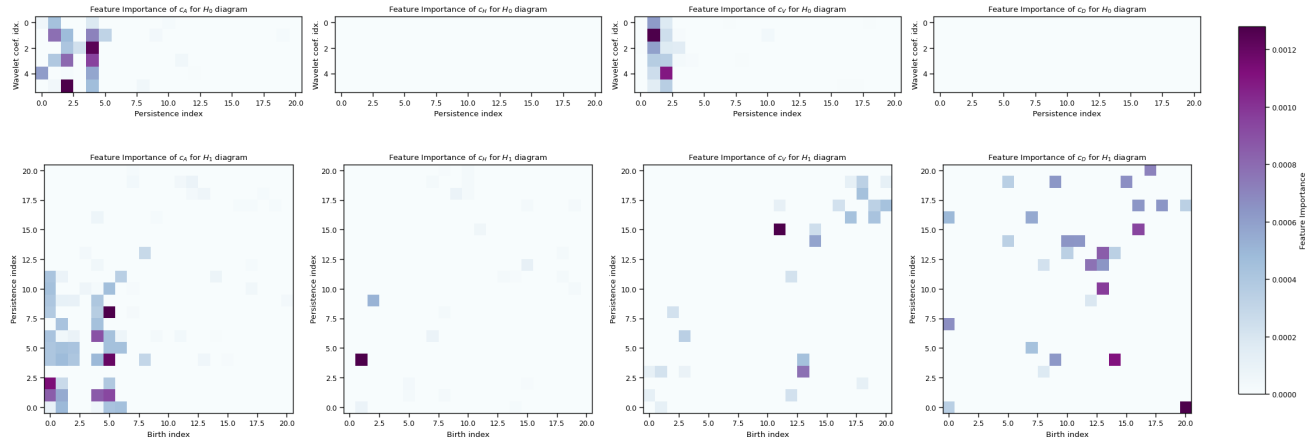


Figure 5: Importance of the coefficients of the QUPID-coif2 vectorization for the classification task CD68⁺ vs FoxP3⁺.

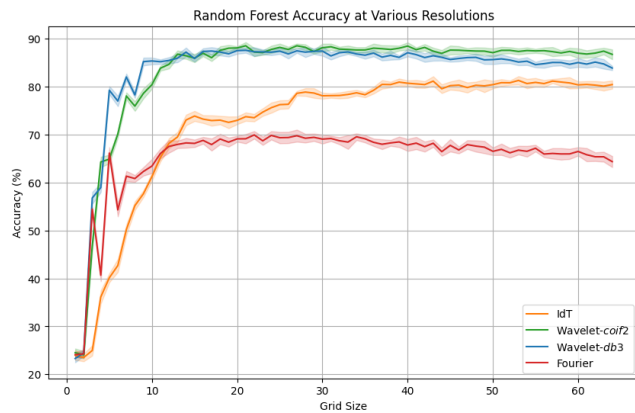


Figure 6: Influence of the resolution parameter on the accuracy for classifying the ORBIT5K dataset.

Fourier and wavelet transforms allows for a certain robustness to a resolution loss, successfully compressing the topological information.

- By its simplicity, we claim that we have developed a white-box algorithm allowing for immediate interpretability. This property becomes extremely valuable when working on real-world data.

Using discrete transforms to analyze topological descriptors is a research direction of growing interest, both theoretically; see [47] and experimentally; see [27]. In the present paper, we have benefitted from the meagre computational cost of our algorithm to optimize over the best integral transform and grid parameters. Future works involving finer qualitative approaches to better understand which transform is more suited to a given type of data would be essential. Finally, we point

out that QUPID is perfectly suited for the vectorization of many recent invariants of multiparameter persistent homology, which take the form of discrete measures in the plane [48]. We defer the study of QUPID in such multiparameter analyses for future work.

References

- [1] Bastian Rieck, Tristan Yates, Christian Bock, Karsten Borgwardt, Guy Wolf, Nicholas Turk-Browne, and Smita Krishnaswamy. Uncovering the topology of time-varying fmri data using cubical persistence. *Advances in neural information processing systems*, 33:6900–6912, 2020.
- [2] Ximena Fernández and Diego Mateos. Topological biomarkers for real-time detection of epileptic seizures. *arXiv preprint arXiv:2211.02523*, 2022.
- [3] Andrew Aukerman, Mathieu Carrière, Chao Chen, Kevin Gardner, Raúl Rabadán, and Rami Vanguri. Persistent homology based characterization of the breast cancer immune microenvironment: a feasibility study. *Journal of Computational Geometry*, 12(2):183–206, 2022.
- [4] Takashi Ichinomiya, Ippei Obayashi, and Yasuaki Hiraoka. Protein-folding analysis using features obtained by persistent homology. *Biophysical Journal*, 118(12):2926–2937, 2020.
- [5] Raúl Rabadán and Andrew J Blumberg. *Topological data analysis for genomics and evolution: topology in biology*. Cambridge University Press, 2019.
- [6] Yongjin Lee, Senja D Barthel, Paweł Dłotko, S Mo-hamad Moosavi, Kathryn Hess, and Berend Smit. Quantifying similarity of pore-geometry in nanoporous materials. *Nature communications*, 8(1):1–8, 2017.
- [7] Yasuaki Hiraoka, Takenobu Nakamura, Akihiko Hirata, Emerson G Escobar, Kaname Matsue, and Yasumasa Nishiura. Hierarchical structures of amor-

- phous solids characterized by persistent homology. *Proceedings of the National Academy of Sciences*, 113(26):7035–7040, 2016.
- [8] Pratyush Pranav, Herbert Edelsbrunner, Rien Van de Weygaert, Gert Vegter, Michael Kerber, Bernard JT Jones, and Mathijs Wintraecken. The topology of the cosmic web in terms of persistent betti numbers. *Monthly Notices of the Royal Astronomical Society*, 465(4):4281–4310, 2017.
- [9] Alberto Alcalá-Alvarez and Pablo Padilla-Longoria. A framework for topological music analysis (tma). *Journal of Mathematics and Music*, 18(1):139–172, 2024.
- [10] Martín Mijangos, Alessandro Bravetti, and Pablo Padilla-Longoria. Musical stylistic analysis: a study of intervallic transition graphs via persistent homology. *Journal of Mathematics and Music*, 18(1):89–108, 2024.
- [11] Charles R Qi, Hao Su, Kaichun Mo, and Leonidas J Guibas. Pointnet: Deep learning on point sets for 3d classification and segmentation. In *Proceedings of the IEEE conference on computer vision and pattern recognition*, pages 652–660, 2017.
- [12] Caroline Moosmüller and Alexander Cloninger. Linear optimal transport embedding: provable wasserstein classification for certain rigid transformations and perturbations. *Information and Inference: A Journal of the IMA*, 12(1):363–389, 2023.
- [13] Varun Khurana, Harish Kannan, Alexander Cloninger, and Caroline Moosmüller. Supervised learning of sheared distributions using linearized optimal transport. *Sampling Theory, Signal Processing, and Data Analysis*, 21(1):1, 2023.
- [14] Olympio Hacquard, Gilles Blanchard, and Clément Levrard. Statistical learning on measures: an application to persistence diagrams. *arXiv preprint arXiv:2303.08456*, 2023.
- [15] Henry Adams, Tegan Emerson, Michael Kirby, Rachel Neville, Chris Peterson, Patrick Shipman, Sofya Chepushtanova, Eric Hanson, Francis Motta, and Lori Ziegelmeier. Persistence images: a stable vector representation of persistent homology. *Journal of Machine Learning Research*, 18(8):1–35, 2017.
- [16] Mathieu Carrière, Marco Cuturi, and Steve Oudot. Sliced wasserstein kernel for persistence diagrams. In *International Conference on Machine Learning*, volume 70, pages 664–673, Jul 2017.
- [17] Tam Le and Makoto Yamada. Persistence fisher kernel: A riemannian manifold kernel for persistence diagrams. In *Advances in Neural Information Processing Systems*, pages 10027–10038, 2018.
- [18] Mathieu Carriere, Frederic Chazal, Yuichi Ike, Theo Lacombe, Martin Royer, and Yuhei Umeda. Perslay: A neural network layer for persistence diagrams and new graph topological signatures. In Silvia Chiappa and Roberto Calandra, editors, *Proceedings of the Twenty Third International Conference on Artificial Intelligence and Statistics*, volume 108 of *Proceedings of Machine Learning Research*, pages 2786–2796. PMLR, 26–28 Aug 2020.
- [19] Raphael Reinauer, Matteo Caorsi, and Nicolas Berkouk. Persformer: A transformer architecture for topological machine learning. *CoRR*, abs/2112.15210, 2021.
- [20] Martin Royer, Frederic Chazal, Clément Levrard, Yuhei Umeda, and Yuichi Ike. Atol: Measure vectorization for automatic topologically-oriented learning. In Arindam Banerjee and Kenji Fukumizu, editors, *Proceedings of The 24th International Conference on Artificial Intelligence and Statistics*, volume 130 of *Proceedings of Machine Learning Research*, pages 1000–1008. PMLR, 13–15 Apr 2021.
- [21] Herbert Edelsbrunner and John L Harer. *Computational topology: an introduction*. American Mathematical Society, 2022.
- [22] Jean-Daniel Boissonnat, Frédéric Chazal, and Mariette Yvinec. *Geometric and topological inference*, volume 57. Cambridge University Press, 2018.
- [23] Frédéric Chazal, Vin de Silva, Marc Glisse, and Steve Oudot. *The structure and stability of persistence modules*. SpringerBriefs in Mathematics. Springer, 2016.
- [24] Vincent Divol and Théo Lacombe. Understanding the topology and the geometry of the space of persistence diagrams via optimal partial transport. *arXiv preprint arXiv:1901.03048*, 2019.
- [25] Felix Hensel, Michael Moor, and Bastian Rieck. A survey of topological machine learning methods. *Frontiers in Artificial Intelligence*, 4:681108, 2021.
- [26] Peter Bubenik, Michael Hull, Dhruv Patel, and Benjamin Whittle. Persistent homology detects curvature. *Inverse Problems*, 36(2):025008, 23, 2020.
- [27] Olympio Hacquard and Vadim Lebovici. Euler characteristic tools for topological data analysis. 2023.
- [28] Stéphane Mallat. *A wavelet tour of signal processing*. Elsevier/Academic Press, Amsterdam, third edition, 2009. The sparse way, With contributions from Gabriel Peyré.
- [29] James W. Cooley and John W. Tukey. An algorithm for the machine calculation of complex fourier series. *Mathematics of computation*, 19(90):297–301, 1965.
- [30] Ingrid Daubechies. *Ten Lectures on Wavelets*. Society for Industrial and Applied Mathematics, 1992.
- [31] Gregory Beylkin, Ronald Coifman, and Vladimir Rokhlin. Fast wavelet transforms and numerical algorithms i. *Communications on pure and applied mathematics*, 44(2):141–183, 1991.
- [32] D Yogeshwaran, Eliran Subag, and Robert J Adler. Random geometric complexes in the thermodynamic regime. *Probability Theory and Related Fields*, 167:107–142, 2017.
- [33] Ulrich Bauer and Herbert Edelsbrunner. The Morse theory of čech and Delaunay complexes. *Trans. Amer. Math. Soc.*, 369(5):3741–3762, 2017.
- [34] Raimund Seidel. The upper bound theorem for polytopes: an easy proof of its asymptotic version. *Comput. Geom.*, 5(2):115–116, 1995.

- [35] Nikola Milosavljević, Dmitriy Morozov, and Primoz Skraba. Zigzag persistent homology in matrix multiplication time. In *Proceedings of the twenty-seventh Annual Symposium on Computational Geometry*, pages 216–225, 2011.
- [36] Clément Maria, Jean-Daniel Boissonnat, Marc Glisse, and Mariette Yvinec. The gudhi library: Simplicial complexes and persistent homology. In *Mathematical Software–ICMS 2014: 4th International Congress, Seoul, South Korea, August 5–9, 2014. Proceedings 4*, pages 167–174. Springer, 2014.
- [37] Leo Breiman. Random forests. *Machine learning*, 45:5–32, 2001.
- [38] Fabian Pedregosa, Gaël Varoquaux, Alexandre Gramfort, Vincent Michel, Bertrand Thirion, Olivier Grisel, Mathieu Blondel, Peter Prettenhofer, Ron Weiss, Vincent Dubourg, et al. Scikit-learn: Machine learning in python. *the Journal of machine Learning research*, 12:2825–2830, 2011.
- [39] Jian Sun, Maks Ovsjanikov, and Leonidas Guibas. A concise and provably informative multi-scale signature based on heat diffusion. In *Computer graphics forum*, volume 28, pages 1383–1392. Wiley Online Library, 2009.
- [40] Quoc Hoan Tran, Van Tuan Vo, and Yoshihiko Hasegawa. Scale-variant topological information for characterizing complex networks. *arXiv preprint arXiv:1811.03573*, 2018.
- [41] Zhen Zhang, Mianzhi Wang, Yijian Xiang, Yan Huang, and Arye Nehorai. Retgk: Graph kernels based on return probabilities of random walks. In *Advances in Neural Information Processing Systems*, pages 3968–3978, 2018.
- [42] Saurabh Verma and Zhi-Li Zhang. Hunt for the unique, stable, sparse and fast feature learning on graphs. In *Advances in Neural Information Processing Systems*, pages 88–98, 2017.
- [43] Xinyi Zhang and Lihui Chen. Capsule graph neural network. In *International Conference on Learning Representations*, 2019.
- [44] Keyulu Xu, Weihua Hu, Jure Leskovec, and Stefanie Jegelka. How powerful are graph neural networks? In *International Conference on Learning Representations (ICLR)*, 2019.
- [45] Peter Bubenik. Statistical topological data analysis using persistence landscapes. *Journal of Machine Learning Research*, 16(3):77–102, 2015.
- [46] Oliver Vipond, Joshua A. Bull, Philip S. Macklin, Ulrike Tillmann, Christopher W. Pugh, Helen M. Byrne, and Heather A. Harrington. Multiparameter persistent homology landscapes identify immune cell spatial patterns in tumors. *Proceedings of the National Academy of Sciences*, 118(41):e2102166118, 2021.
- [47] Konstantin Häberle, Barbara Bravi, and Anthea Monod. Wavelet-based density estimation for persistent homology. *SIAM/ASA Journal on Uncertainty Quantification*, 12(2):347–376, 2024.
- [48] David Loiseaux, Luis Scoccola, Mathieu Carrière, Magnus Bakke Botnan, and Steve Oudot. Stable vectorization of multiparameter persistent homology using signed barcodes as measures. In *Advances in Neural Information Processing Systems*, volume 36, pages 68316–68342. Curran Associates, Inc., 2023.

A Complementary material

This section includes extensive tables that provide a comparative analysis between every transform on the classification tasks of Section 4.

Task		QUPID-fft		QUPID-db1		QUPID-db2		QUPID-db3		QUPID-coif1		QUPID-coif2		QUPID-coif3		QUPID-id	
Dataset	Grid size	Mean	Max	Mean	Max	Mean	Max	Mean	Max	Mean	Max	Mean	Max	Mean	Max	Mean	Max
MUTAG	20 × 20	87.8(±.8)	88.9	87.8(±.8)	88.9	87.8(±.8)	88.9	88.7(±1.0)	90.6	88.6(±.8)	90.0	87.7(±1.2)	90.0	87.5(±.9)	89.4	88.1(±.7)	89.4
	32 × 32	89.1(±1.2)	91.1	88.4(±1.3)	90.0	88.6(±1.0)	90.0	88.9(±1.0)	90.6	88.9(±.7)	90.0	89.7(±.5)	90.6	89.8(±.9)	91.7	89.1(±.9)	90.7
	50 × 50	88.1(±1.1)	89.4	86.9(±1.1)	88.9	87.6(±.9)	88.9	88.3(±1.4)	91.1	88.2(±.9)	89.4	88.3(±1.1)	90.0	88.1(±.6)	88.9	87.4(±1)	88.9
DHFR	20 × 20	77.8(±.7)	78.9	77.8(±.6)	78.9	78.3(±.7)	78.9	79.3(±.6)	80.0	78.5(±.6)	79.6	79.2(±1.0)	81.2	79.0(±.8)	80.4	78.7(±.9)	79.7
	32 × 32	79.1(±1.0)	80.5	81.5(±.7)	83.1	81.8(±.7)	82.9	81.1(±1.0)	82.4	81.4(±.5)	82.1	80.7(±.5)	82.4	80.6(±.7)	81.9	81.1(±.5)	82.0
	50 × 50	79.6(±.7)	81.2	80.6(±.4)	81.2	80.2(±.4)	80.8	80.7(±.4)	81.5	81.0(±.5)	81.9	81.5(±.5)	82.3	80.9(±.9)	82.7	81.2(±.7)	82.7
COX2	20 × 20	78.3(±.6)	78.9	79.2(±.7)	80.4	79.7(±.7)	81.1	79.7(±.7)	80.9	80.0(±.4)	80.4	79.7(±.5)	80.4	79.5(±.8)	81.5	79.4(±.7)	80.4
	32 × 32	76.7(±.7)	77.8	77.3(±1.0)	79.3	78.0(±1.0)	79.3	78.0(±1.1)	79.3	78.0(±.6)	78.9	78.2(±.6)	78.9	77.4(±.8)	78.5	77.5(±.5)	78.5
	50 × 50	77.1(±.9)	78.3	77.5(±.7)	78.5	78.2(±.5)	78.9	77.7(±.6)	78.9	78.7(±.7)	80.0	78.2(±1.0)	79.3	78.8(±1.2)	80.2	78.0(±.4)	78.5
PROTEINS	20 × 20	72.5(±.6)	73.2	72.4(±.4)	72.8	72.5(±.7)	73.4	72.6(±.6)	73.4	72.8(±.6)	73.6	72.3(±.5)	73.0	72.1(±.4)	72.9	71.9(±.7)	73.2
	32 × 32	71.9(±.5)	72.8	72.1(±.5)	72.9	72.3(±.5)	73.1	72.3(±.5)	73.3	72.3(±.6)	73.4	71.9(±.5)	73.0	72.1(±.8)	73.0	72.2(±.5)	73.2
	50 × 50	71.9(±.6)	72.7	72.1(±.5)	73.1	72.4(±.6)	73.2	72.4(±.6)	73.2	72.7(±.5)	73.5	72.6(±.5)	73.5	72.6(±.5)	73.3	71.4(±.4)	72.1
IMDB-B	20 × 20	67.6(±.6)	68.6	67.5(±.8)	68.7	67.1(±.6)	68.3	67.0(±.6)	67.7	67.1(±.3)	67.5	66.8(±.7)	67.9	66.4(±.9)	68.3	67.2(±.7)	68.3
	32 × 32	66.7(±.5)	67.7	66.4(±.9)	68.3	66.9(±.8)	67.9	67.2(±.6)	67.9	66.7(±.8)	67.7	66.8(±.6)	67.7	66.8(±.6)	67.8	66.5(±.6)	67.9
	50 × 50	67.5(±.8)	69.1	68.2(±.6)	69.3	68.1(±.7)	69.2	67.4(±.8)	68.5	68.2(±.7)	69.1	67.7(±.4)	68.3	67.7(±.5)	68.5	66.7(±.9)	67.9
IMDB-M	20 × 20	42.2(±.5)	43.1	42.4(±.4)	42.9	42.2(±.5)	42.9	42.5(±.3)	43.3	42.3(±.7)	43.5	42.3(±.3)	42.8	42.5(±.4)	43.2	42.8(±.4)	43.6
	32 × 32	42.8(±.5)	43.7	42.8(±.5)	43.9	42.5(±.4)	43.5	43.1(±.5)	43.9	42.9(±.5)	43.6	42.7(±.4)	43.5	42.6(±.5)	43.8	43.1(±.5)	44.3
	50 × 50	42.9(±.5)	43.7	42.9(±.2)	43.3	43.0(±.5)	43.6	43.3(±.6)	44.4	43.1(±.5)	43.9	43.7(±.5)	43.9	43.3(±.4)	44.1	43.1(±.4)	43.7
COLLAB	10 × 10	86.1(±.9)	86.3	85.7(±.9)	85.9	86.0(±.2)	86.3	86.0(±.6)	86.3	86.0(±.6)	86.2	86.1(±.2)	86.3	85.9(±.2)	86.3	85.7(±.1)	85.9
	20 × 20	86.4(±1.1)	86.5	86.0(±.2)	86.3	86.2(±.2)	86.4	86.3(±.2)	86.6	86.3(±.1)	86.5	86.3(±.1)	86.7	86.3(±.2)	86.6	86.0(±.2)	86.3
	10 × 10	65.6(±.2)	65.9	65.8(±.1)	65.9	66.1(±.2)	66.5	65.8(±.3)	66.2	65.7(±.3)	66.2	65.6(±.3)	66.2	65.6(±.2)	65.9	65.5(±.3)	66.1
REDDIT-5K	20 × 20	65.8(±.2)	66.2	65.9(±.2)	66.2	66.0(±.3)	66.6	65.9(±.3)	66.4	65.6(±.2)	66.0	66.0(±.3)	66.5	65.6(±.2)	65.8	65.2(±.2)	65.5
	10 × 10	51.4(±.1)	51.7	50.8(±.1)	51.1	51.1(±.2)	51.6	51.3(±.2)	51.6	51.2(±.2)	51.8	51.0(±.2)	51.4	51.0(±.2)	51.3	49.1(±.3)	49.8
	20 × 20	51.0(±.2)	51.3	49.0(±.2)	(49.6)	50.1(±.3)	50.5	50.5(±.2)	50.8	50.4(±.2)	50.8	50.3(±.2)	50.7	50.0(±.3)	50.4	47.0(±.2)	47.4

Table 5: Comparative analysis of graph data classification scores of the methods presented in this study.

Task	QUPID-fft	QUPID-db1	QUPID-db2	QUPID-db3	QUPID-coif1	QUPID-coif2	QUPID-coif3	QUPID-id
ORBIT5K	69.2(±.7)	82.0(±1.0)	87.9(±.8)	88.2(±.7)	87.9(±.6)	88.3(±.4)	87.6(±.3)	82.0 ±.6

Table 6: Comparative analysis of ORBIT5K classification scores for several choice of discrete transforms.

Task	Classifier	Transformation	QUPID-fft	QUPID-db1	QUPID-db2	QUPID-db3	QUPID-coif1	QUPID-coif2	QUPID-coif3	QUPID-coif4	QUPID-id
CD68 ⁺ vs CD8 ⁺	RFC	PD	69.1	71.6	74.1	76.5	74.6	74.8	77.3	79.0	69.9
	LDA	PD	63.4	64.5	64.3	60.0	61.1	66.3	59.5	57.7	63.2
	RFC	Raw	52.1	55.8	51.8	53.6	58.2	58.6	59.5	60.2	52.7
	LDA	Raw	48.4	62.5	62.8	64.5	61.4	65.0	63.9	60.0	61.4
CD68 ⁺ vs FoxP3 ⁺	RFC	PD	94.3	91.7	94.3	94.8	96.2	96.8	98.2	97.0	91.7
	LDA	PD	94.5	87.8	86.5	90.3	88.0	91.5	88.7	89.0	90.0
	RFC	Raw	87.2	89.0	87.7	86.0	87.8	84.7	84.8	88.2	89.2
	LDA	Raw	64.3	85.8	86.8	84.8	86.8	85.3	88.5	86.5	88.3
CD8 ⁺ vs FoxP3 ⁺	RFC	PD	91.7	89.1	89.1	90.5	94.5	92.7	95.2	96.3	90.7
	LDA	PD	85.2	80.9	80.7	77.7	82.3	80.0	80.7	82.7	82.7
	RFC	Raw	83.0	86.6	87.1	86.6	84.5	85.9	85.7	87.7	83.8
	LDA	Raw	68.0	82.1	84.0	84.3	85.4	84.8	84.3	87.0	85.9
All classes	RFC	PD	72.6	67.4	72.7	74.7	78.1	78.0	77.5	79.4	68.8
	LDA	PD	67.9	59.5	61.7	58.4	61.4	60.3	56.1	56.9	47.1
	RFC	Raw	59.2	60.8	60.2	62.9	62.7	62.7	63.8	66.2	62.0
	LDA	Raw	41.0	64.9	67.0	65.6	65.6	66.5	67.7	67.2	67.9

Table 7: Comparative analysis of immune cells classification for several choices of discrete transforms on Persistence diagrams and raw points with RandomForestClassifier (RFC) and LinearDiscriminantAnalysis (LDA).